Water Resources Research

RESEARCH ARTICLE
10.1029/2020WR027511

Key Points:
- Unidirectional multirate tracer experiments are conducted in one sandstone and two carbonate samples
- Nonequilibrium transport effects in carbonates are uncovered through the application of the CTRW formulation
- We have estimated the characteristic length scales associated with mixing and unresolved heterogeneities

Supporting Information:
- Supporting Information S1

Correspondence to:
R. Pini,
r.pini@imperial.ac.uk

Citation:
Kurotori, T., Zahasky, C., Benson, S. M., & Pini, R. (2020). Description of chemical transport in laboratory rock cores using the continuous random walk formalism. *Water Resources Research*, *56*, e2020WR027511. https://doi.org/10.1029/2020WR027511

Received 17 MAR 2020
Accepted 11 SEP 2020
Accepted article online 16 SEP 2020

Description of Chemical Transport in Laboratory Rock Cores Using the Continuous Random Walk Formalism

Takeshi Kurotori[1], Christopher Zahasky[2,3], Sally M. Benson[2], and Ronny Pini[1]

[1]Department of Chemical Engineering, Imperial College London, London, UK, [2]Department of Energy Resources Engineering, Stanford University, Stanford, CA, USA, [3]Department of Geoscience, University of Wisconsin-Madison, Madison, WI, USA

Abstract We investigate chemical transport in laboratory rock cores using unidirectional pulse tracer experiments. Breakthrough curves (BTCs) measured at various flow rates in one sandstone and two carbonate samples are interpreted using the one-dimensional Continuous Time Random Walk (CTRW) formulation with a truncated power law (TPL) model. Within the same framework, we evaluate additional memory functions to consider the Advection-Dispersion Equation (ADE) and its extension to describe mass exchange between mobile and immobile solute phases (Single-Rate Mass Transfer model, SRMT). To provide physical constraints to the models, parameters are identified that do not depend on the flow rate. While the ADE fails systematically at describing the effluent profiles for the carbonates, the SRMT and TPL formulations provide excellent fits to the measurements. They both yield a linear correlation between the dispersion coefficient and the Péclet number ($D_L \propto \mathrm{Pe}$ for $10 < \mathcal{O}(\mathrm{Pe}) < 100$), and the longitudinal dispersivity is found to be significantly larger than the equivalent grain diameter, D_e. The BTCs of the carbonate rocks show clear signs of nonequilibrium effects. While the SRMT model explicitly accounts for the presence of microporous regions (up to 30% of the total pore space), in the TPL formulation the time scales of both advective and diffusive processes ($t_1(\mathrm{Pe})$ and t_2) are associated with two characteristic heterogeneity length scales ($\bar{d}$ and l, respectively). We observed that $l \approx 2.5 \times D_e$ and that anomalous transport arises when $l/\bar{d} \leq \mathcal{O}(1)$. In this context, the SRMT and TPL formulations provide consistent, yet complementary, insight into the nature of anomalous transport in laboratory rock cores.

1. Introduction

The study of chemical transport in porous media finds application in a range of engineering problems, many of which occur in natural environments. Traditionally, in situ soil remediation, nuclear waste disposal, and enhanced hydrocarbon recovery have largely contributed to advancements in this area, which continues to grow through the development of emerging technologies, such as geologic CO_2 sequestration. Transport is a fundamental component in the analysis of these systems, because it provides the driving force for the physical and chemical interactions that take place between the fluid and the rock (Steefel & Maher, 2009). However, natural porous media are disordered, with chemical and physical properties that can vary in both space and in time, and over a wide range of length and temporal scales (Ringrose et al., 1993). In practice, this disorder leads to the appearance of heterogeneous velocity fields, which generate concentration distributions of the solutes that are complex and difficult to predict (Dentz et al., 2011). Our focus with this contribution is on laboratory rock samples and, more specifically, on the interpretation of unidirectional tracer tests that are carried out to quantify their basic transport properties. The analysis of breakthrough curves (BTCs) in laboratory experiments underpins the evaluation of rate-limited mass transfer and the identification of the different mechanisms of mass transfer in rocks (Carrera et al., 1998; Haggerty et al., 2000). In these systems, transport is affected by heterogeneities that initiate at the pore scale (Bijeljic et al., 2011, 2013) and develop toward larger subcore-scale (mm-cm) features, which may or may not be aligned with the main direction of flow (Pini et al., 2016; Silliman & Simpson, 1987; Walsh & Withjack, 1994). Depending on their strength, these heterogeneities can create conditions for which transport of the injected tracer evolves rapidly through preferential flow paths or is retarded by diffusion through microporous domains. The resultant tracer effluent concentration profiles are characterized by early breakthrough, strong asymmetry and

tailing at late times, whereby the terms "anomalous" or "non-Fickian" have been introduced to describe the associated transport process (Cortis & Berkowitz, 2004; Le Borgne et al., 2011).

Laboratory studies of hydrodynamic dispersion in rocks have been made for many years, but measurements are still sparse, and the values of the obtained transport coefficients are largely scattered. A major driver for this variability is the uncertainty associated with the interpretation of the measurements, which builds on the application of a suitable model to describe the transport of a conservative tracer through the given sample. As anticipated above, the inherent heterogeneity of natural porous media is often brought as the argument to challenge the standard "Fickian" model of transport (Neuman & Tartakovsky, 2009); more precisely, the formulation of the Advection-Dispersion Equation (ADE) that uses a Fickian dispersion model applying the Sheidegger parameterization (Kitanidis, 2017). The latter assumes that the longitudinal dispersion coefficient scales linearly with the mean velocity for large Péclet numbers, that is, $D_L \propto \mathrm{Pe}$ for $\mathcal{O}(\mathrm{Pe}) \sim 10$–$100$. For a unidirectional tracer test, the proportionality constant is given by the longitudinal dispersivity, that is, $D_L = \alpha_L v$, which can therefore be considered as a characteristic length scale of the porous medium (Gist et al., 1990). While it has been shown that for laboratory samples a flow rate independent dispersivity "is often reasonable, at least as a practical approximation" (Kitanidis, 2017), weak-to-moderate nonlinearity has been observed in both experimental and modeling studies on rocks, that is, $D_L \sim \mathrm{Pe}^{\delta}$, with $\delta \geq 1$. Yet, even for the well-studied Berea Sandstone, the value of the power law exponent varies greatly ($\delta = 1.0 - 1.3$) depending on the approach to the modeling (Bijeljic et al., 2004; Honari et al., 2015; Pini et al., 2016). Similar variations are observed on carbonates ($\delta = 1.0 - 1.4$), for which the experimental data set is however more scattered (Bijeljic et al., 2011; Gist et al., 1990; Honari et al., 2015; Kurotori et al., 2019). In this context, studies are needed where experimental observations are made over a wide range of flow rates (or Pe) and where the Sheidegger parameterization is evaluated also in the context of mathematical formulations other than the ADE model.

Various model formulations have been proposed as alternative to the ADE to describe more accurately tracer effluent profiles measured in laboratory studies of dispersion in consolidated rocks. Two important formulations are referred to as multiple rate mass transfer (MRMT; e.g., Haggerty & Gorelick, 1995) and continuous time random walk (CTRW; e.g., Berkowitz et al., 2006). The former is often preferred to the ADE, because of its ability to capture nonequilibrium effects arising from, for example, mass transfer into and out immobile or pseudo-immobile zones (Bretz & Orr, 1987; Grattoni et al., 1987; Honari et al., 2015). However, the basic conditions for its application are not always found in the systems analyzed in the literature, and questions have been raised on the physical meaning of the obtained parameters (Kitanidis, 2017; Pini et al., 2016). This becomes quite apparent when all parameters of the MRMT model are let to change with each individual BTC with the sole intent of obtaining the best match of the experimental data (Khan & Jury, 1990). The predictive capability of such parameterization may be further compromised, because different mechanisms can lead to the same macroscopic effect, such as tailing on the BTC, including matrix diffusion and heterogeneous permeability fields (Carrera et al., 1998). The use of the CTRW approach to laboratory experiments has been largely limited to sandpacks (homogeneous and heterogeneous, e.g., Berkowitz et al., 2006, and references therein) with only very few studies having evaluated its application to consolidated rocks (Bijeljic et al., 2011; Cortis & Berkowitz, 2005), which by the nature of sedimentation and lithification processes contain multiscale heterogeneity. This gap represents an opportunity to expand the operating envelope of the CTRW formalism and to probe the relationship between the parameters of the underlying memory function and experimental variables, such as the flow rate (Berkowitz & Scher, 2009). In this context, it would be highly instructive to apply different expressions of the memory function to experimental breakthrough data in rocks, including formulations that map directly into a MRMT process characterized by diffusive ("first-order") mass transfer processes between mobile and immobile solute phases (Dentz & Berkowitz, 2003).

We report here on a comprehensive set of unidirectional tracer tests carried out in three rock cores with different pore structures, namely, Bentheimer sandstone (BS), Edwards Brown carbonate (EB), and Ketton limestone (KL). The experiments have been carried out over a range of large Péclet numbers ($\mathcal{O}(\mathrm{Pe}) \sim 10 - 100$), and the measured BTCs have been interpreted using the CTRW formalism that uses a truncated power law (TPL) distribution for the transition time. Two additional expressions for the memory function are considered to evaluate transport models that are formally equivalent to those commonly adopted in the literature, namely, the ADE and a single-rate, first-order mass transfer (SRMT) model to approximate diffusive trapping. In the application of the three models, we have adopted an approach that aims at minimizing the number of fitting parameters relative to most analyses presented in the literature. In particular, we have

Table 1
Properties of the Samples Used for the Pulse-Tracer Tests

	Ketton limestone	Edwards carbonate	Bentheimer sandstone
ϕ_t [–]	0.23 (0.27)	0.41 (0.46)	0.25 (0.24)
K [D]	1.9 ± 0.1	0.13 ± 0.01	1.7 ± 0.1
ρ_{sk} [g cm^{-3}]	2.77	2.85	2.64
ρ_b [g cm^{-3}]	2.01	1.55	2.01
R_p μm	42.5	10.5	17.5
D_e μm	541	391	257
Ψ [–]	0.82	0.53	0.63

Note. All quantities are defined in the Notation section, while details on the measurements are described in section 2.2.

kept constant those parameters that do not depend on the flow rate, including the longitudinal dispersivity, thereby addressing the key question of whether or not we can capture the behavior of different BTCs in each rock using the Sheidegger approximation. A systematic comparison of the parameterization achieved for TPL and SMRT formulations carried out to provide additional insight on the complementarity of these two approaches.

2. Experimental

2.1. Rock Samples

Three 10-cm-long and 5-cm-diameter rock cores were used in the experiments, namely, KL (Ketton Quarry, Rutland, UK), BS, and EB (both sourced from Kocurek Industries INC, Caldwell, TX, USA). Table 1 summarizes various petrophysical properties of the samples. A porosity profile along the each sample was measured using a clinical X-ray CT instrument at a resolution of 2 mm (see Figure S1 in the supporting information). The obtained profiles show negligible fluctuations (<2 %rel), and the porosity is therefore considered constant in the modeling. The core-averaged porosity, ϕ_t, differs among the samples and takes the following values: 23.3 % (KL), 41.3 % (EB), and 25.1 % (BS). The average porosity is not correlated to the measured sample permeability, which decreases in the order KL (1,900 mD) > BS (1,700 mD) > EB (132 mD). The latter was measured upon application of Darcy's law to multirate injection tests conducted with water in the range of flow rates, q = 2–19 ml/min (Figure S2). The remaining petrophysical properties listed in Table 1 have been measured on smaller plugs drilled from a section adjacent to the main rock core, as described in the following section.

2.2. Petrophysical Properties on mm Plugs

Up to six small cylindrical plugs (10 mm long, 8 mm diameter) were drilled from the main rock core and used for further characterization in the following order: (i) micron-resolution imaging by X-ray CT for grain-size distribution analysis (using a ZEISS XRadia 500 3-D microscope); (ii) Helium pycnometry for estimating the plug skeletal density (experiments conducted at 25°C and 135 kPa using a Micromeritics AccuPyc II 1340); and (iii) mercury intrusion porosimetry (MIP) for estimating the plug bulk density and for pore-throat size distribution analysis (experiments conducted in the pressure range from vacuum to 22.8 MPa using a Micromeritics Autopore IV 9500). The average values of the skeletal (ρ_{sk}) and bulk density (ρ_b) of the three rocks have been combined to provide an independent estimate of the total sample porosity, $\phi_t = 1 - \rho_b/\rho_{sk}$. These results are denoted by the values in parentheses in Table 1 and indicate a slight overestimation (2–8 %rel.) as compared to values obtained on the large cores by X-ray CT.

Three-dimensional reconstructions of a $(3 \times 3 \times 3)$ mm^3 subvolume of each plug are shown in Figure 1 (middle panel) together with a representative gray-scale 2-D horizontal cross section extracted from the 3-D volume (right panel). Details of the tomography acquisition protocol and of the image processing workflow (carried out using Avizo-9, Thermo Fisher Scientific) are described in section S3.4. The 2-D and 3-D tomograms reveal the distinct pore-scale features of the three rocks: BS is fairly well sorted and possesses angular grains; KL is composed of smooth spherical grains (ooids), while EB includes a more disordered structure with well-developed vuggy porosity. The grain-size distribution extracted from the 3-D data set of each rock is shown in the histograms plots (left panel) in terms of the equivalent grain diameter, $d_e = (6V_g/\pi)^{1/3}$,

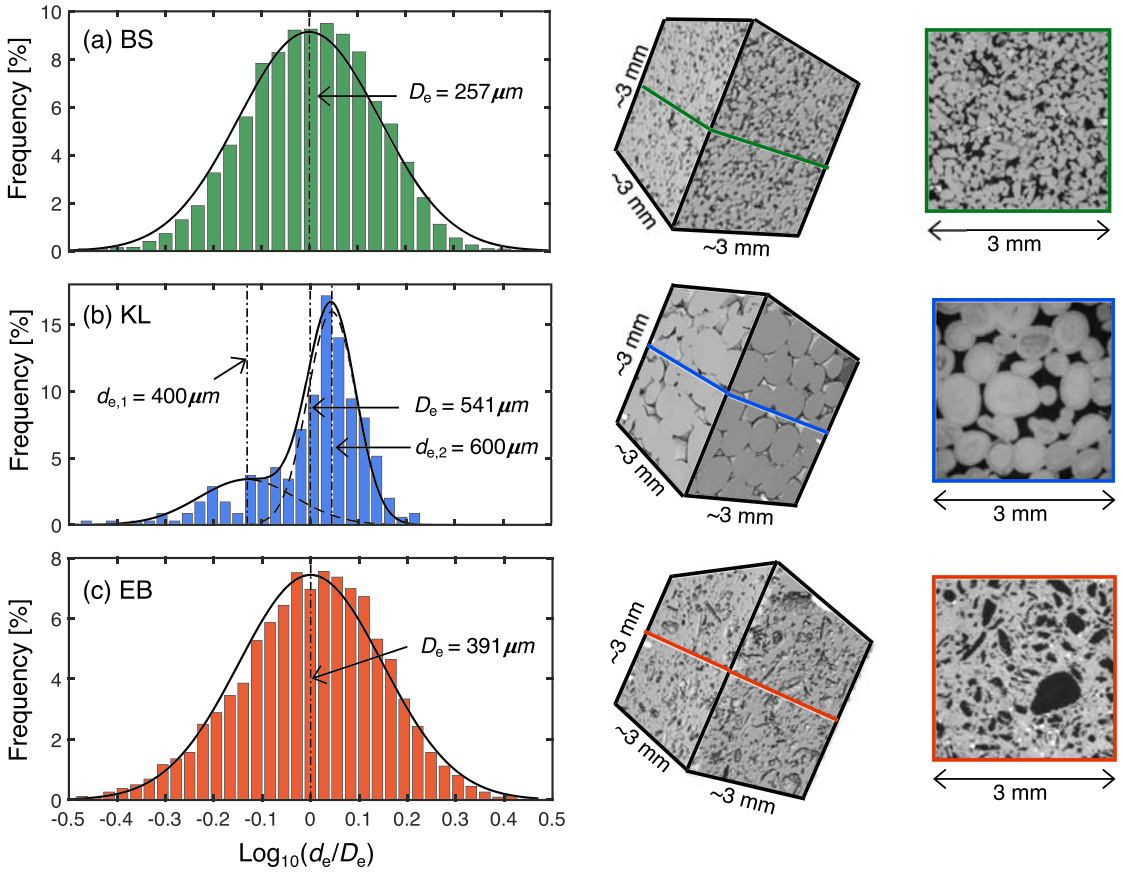

Figure 1. Histograms of the grain-size distributions of (a) BS, (b) KL, and (c) EB extracted from a $(3 \times 3 \times 3)$ mm^3 subvolume of the rock plug imaged by X-ray microCT (middle panel), corresponding to about 1,000 particles for KL and 4000 particles for BS and EB. Two-dimensional horizontal cross sections are also shown in the figure (right panel).

where V_g is the volume of a given grain extracted from the microCT images. Both BS and EB yield lognormal distributions centered around a mean grain diameter of $D_e = 257$ and 391 μm, respectively, but with a similar width ($\sigma_{std} \approx 0.148$). The grain-size distribution of KL is narrower and bimodal with maxima observed at $d_{e,1} = 400\,\mu m$ and $d_{e,1} = 610\,\mu m$, respectively. These two grain classes contribute to 30% and 70% of the total distribution yielding a mean value of $D_e = 541\,\mu m$. The average grain's sphericity index Ψ computed from the images decreases in the order KL (0.82) > BS (0.63) > EP (0.53). The latter is defined as the ratio between two surface areas values, namely, the value for a sphere with the same grain volume and the actual value.

In Figure 2 the pore-throat size distribution curves obtained on the three rocks by MIP are shown. These are composite curves that have been obtained upon combining the curves measured on the mm plugs for each rock sample and are therefore representative of a sample with volume of 2–3 cm^3. Details on the construction of the curves are provided in section S3.3. The distribution of BS is largely unimodal with a single distinct peak at 17.5 μm. In contrast, the two carbonate samples (EB and KL) exhibit a bimodal distribution. For EB the peak at large radii is found at 10.5 μm and is quite broad (0.1–20 μm), reflecting the complexity of the pore structure of this carbonate rock. For KL, the peak at large radii (42.5 μm) is attributed to interparticle pores, while the peak at small radii is attributed to intraparticle pores (0.01–0.1 μm). It is worth noting that all three rocks possess a nonnegligible fraction of submicron porosity ($r_p^m < 1\,\mu m$) that increases in the order BS (5 %) < EB (10 %) < KL (33 %), as computed from the ratio of the corresponding area under the curve, that is, $\phi_{mi}/\phi_t = \int_0^{r_p^m} f(r_p) dr_p$.

2.3. Pulse-Tracer Tests

Pulse-tracer tests were carried out on the three water-saturated rock cores over a range of flow rates (q = 2 − 19 ml/min) and at ambient pressure and temperature conditions (Tables S1–S3). For the experiments, a custom-built core-flooding apparatus was used that is described in detail in a previous publication

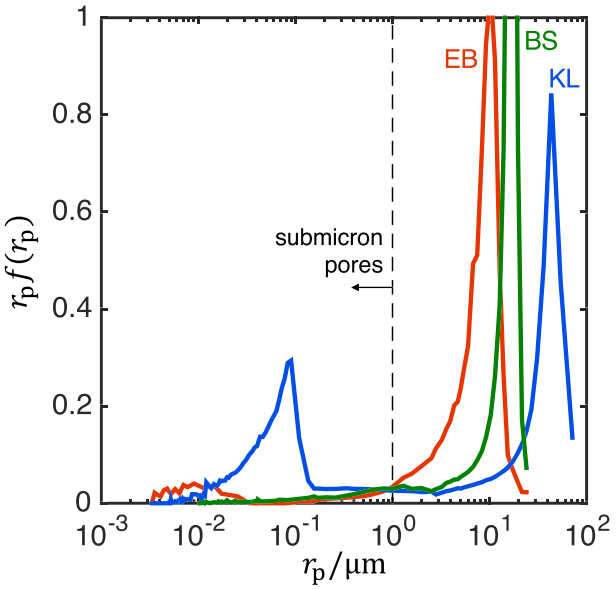

Figure 2. Pore-throat size distribution, $r_p f(r_p)$, as a function of the pore-throat radius, r_p, for BS, KL, and EB, as determined by MIP experiments. The peak at large radii is used to define the mean pore-throat radius, R_p, reported in Table 1.

(Kurotori et al., 2019). Briefly, the main components of the experimental system are (i) the high-pressure aluminum core-holder (Figure S3); (ii) a differential pressure transducer (Keller UK, model PRD-33X, accuracy: 0.05%FS) connected to the inlet and outlet faces of the sample; (iii) radioactivity detectors mounted upstream and downstream of the core holder (Carroll and Ramsey Associates, USA) to measure inlet and effluent concentration of the radio tracer (or conductivity microflow cells, Model 829 by Amber Scientific, USA, when a brine-tracer is used); (iv) three high-pressure syringe pumps (Teledyne ISCO, Model 1000D) for continuous delivery of carrier fluid, for maintaining constant confining pressure and for maintaining a back-pressure, respectively); and one two-way valve for tracer injection (Cheminert, HPLC 6 port injection valve, VICI, Thames Restek UK Ltd). During the experiments, real-time logging of the radioactivity (or conductivity) detectors, pressures, and flow rates is achieved by means a Labview (National Instruments) GUI developed in-house.

Prior to mounting it in the core holder, each rock core was dried at a temperature of 60°C for about 100 hr. The cylindrical sample was sandwiched between the two aluminum end caps, and the whole arrangement was jacketed into a heat-shrink FEB sleeve (Polyflon Technology Ltd, UK). The latter was heated carefully to achieve a tight annular seal around the sample and the nitrile o-rings (Barnwell, UK) mounted on both end caps. The aluminum core barrel was then slid on the end caps that were sealed by means of another set of nitrile o-rings and that were subsequently pressed and secured against the sample by two aluminum disks screwed on the barrel (Figure S3). The annular space was then filled with confining fluid (tap water), while maintaining the core holder in vertical position, so as to ensure that any air was removed from the system. The confining pressure was increased gradually to the set value (0.8 MPa for KL and 2.7 MPa for BS and EB). The core holder was then placed horizontally and connected to the pumps by means of PEEK and PTFE tubing (OD 1/16″–1/8″). The system was purged with gaseous CO_2 (0.1–0.2 MPa, purity >99%), followed by the injection of the aqueous carrier solution (tap water) for at least eight pore volumes (PVs) to achieve complete saturation of the pore space. The system was allowed to equilibrate at the given flow rate to reach a stable pressure drop, prior to loading the radio-tracer solution in the sample loop (1 or 2 ml, depending on the experiment). The experiment started by switching the injection valve and was continued for the time equivalent to the injection of 3 PV, while continuously monitoring the concentration of the solution entering and leaving the sample.

The majority of the experiments were conducted using a radio tracer with the radionuclide ^{18}F acting as the active component (half-life, $t_{1/2} = 109.7$ min). The isotope was produced in the chemical form of [18F]FDG (Fluorodeoxyglucose) at the Stanford Medicine Cyclotron Facility and was subsequently dissolved in tap water (with activity concentrations varying between 0.3 and 1.1 mCi/ml and corresponding to $c_{F0} = 2\text{–}7 \times 10^{-13}$ mol/ml). The latter constitutes the radioactive solution injected in the pulse-tracer experiments. [18F]FDG has been demonstrated to behave as a passive tracer in previous studies (Kurotori et al., 2019; Zahasky et al., 2019). The measured activity $c_D(t)$ was corrected to the radioactivity at the injection time, $c(t)$, by accounting for radioactive decay, that is, $c(t) = c_D(t)e^{\eta t}$, where $\eta = \ln(2)/t_{1/2}$. For validation purposes, experiments have also be conducted using a brine tracer (Tables S1 and S3); to this end, potassium chloride (KCl, >99%, Sigma Aldrich) and potassium iodide (KI, 99%, Sigma Aldrich), were used to prepare aqueous, neutrally buoyant carrier (KCl, 7.0 wt%) and tracer (KI, 6.1%) solutions.

3. Modeling

Various physical mechanisms affect the transport of a solute in a laboratory rock core, including local variations in the permeability and porosity, as well as diffusion into/from microporous regions that may act as temporary "traps." Figure 3 shows a snapshot of the three-dimensional map of the solute plume observed experimentally in a microporous carbonate sample (Kurotori et al., 2019), providing direct evidence for the mechanisms just described. The solute plume is significantly deformed through the action of preferential flow pathways and is negatively skewed, with its trailing edge showing signs of retardation. On the

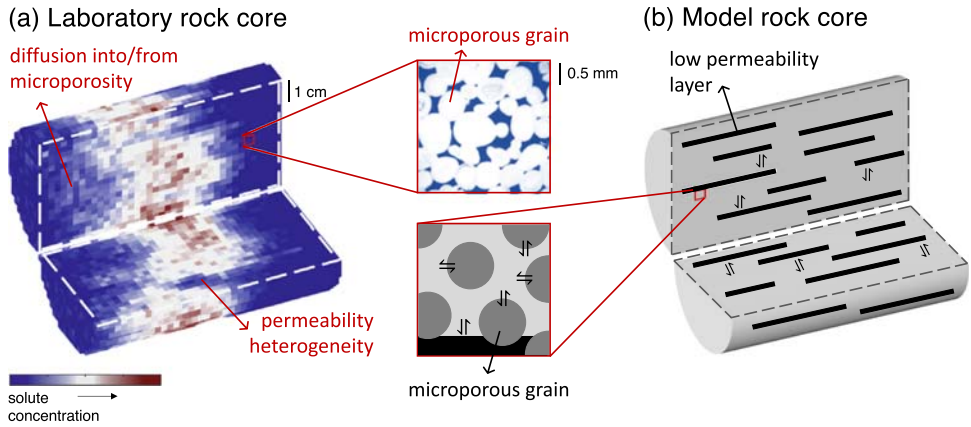

Figure 3. (a) Three-dimensional concentration map of a tracer plume in Ketton Limestone (Kurotori et al., 2019) and (b) conceptualization of the porous medium with subcore-scale heterogeneities in the form of low permeability zones and microporous grains.

right-hand side of the figure, a schematic representation of the porous medium that would give rise to these transport processes and that contains porous grains and zones of low permeability is shown. We use this conceptualization to describe the modeling approach used in this study. We consider a uniformly heterogeneous porous medium, where these features are assumed to overlap and span the whole domain. We therefore adopt a one-dimensional description of transport and use the CTRW formulation to represent these subcore-scale heterogeneities. The model equations are introduced first, followed by the description of the numerical schemes adopted for their solution and the optimization procedure for fitting the experimental BTCs.

3.1. CTRW Model

The CTRW approach describes the transport of solute particles as a stochastic process, where both the length and the time of displacement events are random variables. These are described according to a given distribution, which is used to account for the (unresolved) heterogeneities of the medium and, therefore, for the spatial variability in the pore fluid velocity. The CTRW model is the upscaled representation of this conceptual transport process, which in one-dimension is given by the following integro-differential equation (Berkowitz et al., 2006):

$$\frac{\partial c(z,t)}{\partial t} = -\int_0^t M(t-t')\left[v_\psi \frac{\partial c(z,t')}{\partial z} - D_\psi \frac{\partial^2 c(z,t')}{\partial z^2}\right] dt', \tag{1}$$

where $M(t-t')$ is a so-called memory function that describes displacement events with time steps $t-t'$ through a probability density function (pdf) for the transition time, $\psi(t)$ (see below). The pdf for the transition length of the events is described by a Gaussian distribution and is embedded into the definition of v_ψ and D_ψ, which are the first and second moment of the distribution, respectively (Dentz et al., 2004). These are the counterparts of the "transport velocity" (v) and the "dispersion coefficient" (D_L) used in the classic ADE formulation, but their values may differ ($v = v_\psi$ and $D_L = D_\psi$ for $M = \delta(t-t')$, when Equation 1 reduces to the ADE).

For the numerical treatment of the transport problem, Equation 1 is best formulated in Laplace ($\mathcal{L}$) space (Cortis & Berkowitz, 2005):

$$s\tilde{c}(z,s) - c_0(z) = -\tilde{M}(s)\left[v_\psi \frac{\partial \tilde{c}(z,s)}{\partial z} - D_\psi \frac{\partial^2 \tilde{c}(z,s)}{\partial z^2}\right], \tag{2}$$

where s is the Laplace variable and $\tilde{c}(z,s) = \mathcal{L}\{c(z,t)\}$ is the Laplace transformed concentration. The LHS of Equation 2 represents the time derivative, that is, $\mathcal{L}\{\partial c(z,t)/\partial t\}$, and $c_0(z) = c(z, t=0)$ is the initial condition. The memory function, in the Laplace space, is defined as

$$\tilde{M}(s) = t_1 s \frac{\tilde{\psi}(s)}{1-\tilde{\psi}(s)}, \tag{3}$$

where $\tilde{\psi}(s) = \mathcal{L}\{\psi(t)\}$ can take different forms depending on the physical mechanisms invoked to describe mass transfer in the system under study. We consider the specific case of MRMT that involves first-order mass transfer events between mobile and (pseudo-)immobile solute fractions. The corresponding pdf of transition times in the Laplace Space reads as follows (Berkowitz et al., 2006):

$$\tilde{\psi}(s) = \left[1 + t_1 s\left(1 + \sum_j \frac{\theta_j}{1 + t_{2,j} s}\right)\right]^{-1}, \tag{4}$$

where t_1 is a characteristic time for transport (the average time spend in the mobile zone), $t_{2,j}$ is the release time from the given trap j, and θ_j is the ratio between the volume fraction of the "immobile" zone characterized by $t_{2,j}$ to the volume fraction of the mobile region. For $j = 1$, one obtains a formulation equivalent to the single-rate first-order model that is frequently used in the literature to describe transport of a passive solute in laboratory rock cores—mobile/immobile model (Haggerty & Gorelick, 1995) or capacitance model (Coats et al., 1964); we will use this formulation and refer to it as SRMT. For $\theta = 0$, $\tilde{\psi}(s) = (1 + t_1 s)^{-1}$ is obtained, and the ADE is recovered ($\tilde{M}(s) = 1$).

Because of its flexibility, a TPL is also considered, as suggested previously (Dentz et al., 2004):

$$\tilde{\psi}(s) = (1 + t_2 u)^{\beta} e^{t_1 u} \frac{\Gamma(-\beta, t_1/t_2 + t_1 u)}{\Gamma(-\beta, t_1/t_2)} \quad \text{for} \quad 0 < \beta < 2, \tag{5}$$

where Γ is the incomplete Gamma function. The TPL distribution uses three parameters to describe the transport process, namely, t_1 (the median transition time), t_2 (a so-called cutoff time), and β (the strength of "anomalous" transport behavior). Specifically, for $t_1 \ll t \ll t_2$ and $0 < \beta < 2$ anomalous transport is observed, while for $t \gg t_2$ the transport has evolved to Fickian; systems with $\beta \approx 1.6$ and above are fairly homogeneous (Berkowitz et al., 2006). The cutoff time t_2 can be associated to the largest unresolved heterogeneity length scale l of the porous medium; accordingly, on a scale $H \gg l$ the medium will appear homogeneous, and transport will evolve to normal (Fickian), if the transport processes lead to fully mixed conditions over the length scale l ($t_1 < t_2$). We expect that for the rock cores considered in this study, $H \geq L \gg l$.

We note that while the parameterization of the memory function in the two models appears to be similar, the meaning of the parameters and their effect on the BTC differ. In particular, the parameter β (TPL) and the parameter θ (SRMT) cannot be compared. The former reflects the variability of trapping times and provides for augmented flexibility when fitting the tail of the BTC. On the contrary, in the SRMT the late-time decrease can only be exponential, while θ reflects the volume percentage of immobile zones.

3.2. Numerical Solution Procedure

All tracer tests reported in this study are initiated with the rock sample being saturated with the clean carrier solution and the following initial condition applies:

$$\text{for } t = 0 \text{ and } 0 \leq z \leq L : c = c_0 = 0. \tag{6}$$

Boundary conditions at the core inlet ($z = 0$) and outlet ($z = L$) follow the expressions given by Danckwerts (Fogler, 1999) in the Laplace space:

$$\text{for } z = 0 : \tilde{c}(z = 0) = \tilde{c}_F(s) + \frac{D_\psi}{v_\psi} \left.\frac{\partial \tilde{c}}{\partial z}\right|_{z=0}, \tag{7a}$$

$$\text{for } z = L : 0 = \left.\frac{\partial \tilde{c}}{\partial z}\right|_{z=L}, \tag{7b}$$

where $\tilde{c}_F(s) = c_{F0}(1 - e^{-\epsilon s})/s$ is the flux-averaged concentration at the inlet of the core described by a square input function fitted to the experimental concentration curve measured by the inlet detector, that is, for $\epsilon > t \geq 0 : c_F(t) = c_{F0}$. Here, ϵ is the duration of the square input function, and c_{F0} is the concentration of the injected tracer solution. We note that the Danckwerts boundary conditions correctly represent the experimental system used in this study, where dispersion in the tubing upstream and downstream of the sample is negligibly small.

The set of transport equations of the CTRW model is solved in the Laplace domain by first obtaining the exact analytical solution to Equation 2 for $\tilde{c}(z, s)$ and the given boundary conditions, Equation 7. We report

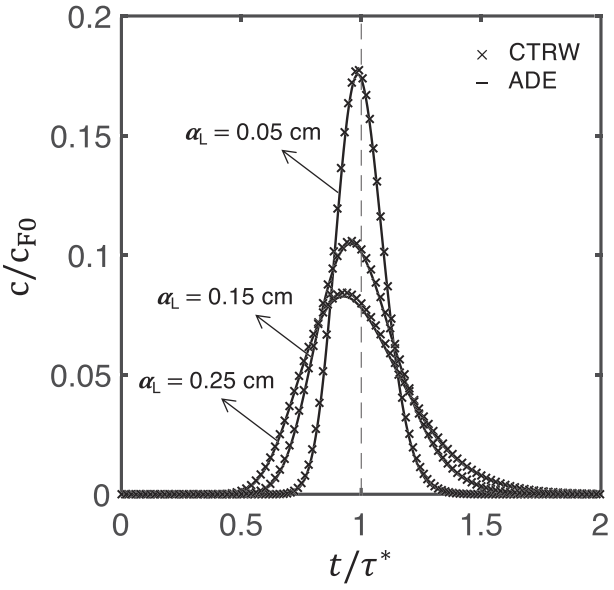

Figure 4. BTCs obtained upon solving the CTRW model presented in section 3.1 for the limiting case of the standard ADE formulation (see section S2). Sample diameter equals 5 cm, length 10 cm, porosity 23%, and volumetric flow rate 10 cm^3/min. The three sets of curves correspond to different values of the longitudinal dispersivity coefficient.

this expression and its derivation in the supporting information (Equation S6 in section S1), as it differs from the solution reported by Cortis and Berkowitz (2005). Accordingly, only the scripts `L_psi.m` and `ilap.m` provided in their CTRW MATLAB toolbox are used here; these are needed to (i) calculate $\tilde{\psi}(s)$ in Equation 3 and (ii) perform the numerical inversion of the Laplace-space solution $\tilde{c}(z,s)$ to the corresponding solution in time domain, $c(z,t)$. All the remaining operations have been carried out using MATLAB routines developed in-house.

3.3. Validation

An assessment is carried out by comparing BTCs generated by the CTRW model for $\tilde{M}(s)=1$ with the numerical solution of the classical ADE formulation (equation and numerical scheme provided in section S2) for a unit square input function with duration $\epsilon = 0.2$ min. We have further assumed a pore velocity $v = v_\psi = 2.21$ cm/min, a porosity $\phi = 0.23$, and a rock of length $L = 10$ cm. Three cases have been run by modifying the longitudinal dispersivity coefficient ($\alpha_\psi = 0.05$, 0.15, and 0.25 cm). The obtained BTCs are plotted in Figure 4 in terms of a normalized concentration (c/c_{F0}) as a function of the reduced time, t/τ^*, where $\tau^* = L/v$. An excellent agreement is observed between the two models over the given range of dispersivity values, which we have chosen so as to cover cases relevant to the rock samples considered in this study. Also, for both models a negligible error (<0.1%) is obtained in the material balance, as estimated from the integral of the BTC relative to the input function, that is, $\int_0^\infty c(z=L,t)dt = c_{F0}\epsilon$.

3.4. Parameters Estimation and Optimization Procedure

The input parameters used to solve the two transport models include the sample properties reported in Table 1, as well as feed radio-tracer concentration, volumetric flow rate, and volume of tracer injected, which are adjusted depending on the experimental conditions (see Tables S1–S3). The remaining set of parameters has been found by fitting the models to the measured BTCs. As explained in the following, we have adopted an approach that aims at minimizing the number of fitting parameters relative to most analyses presented in the literature. For the SRMT model, the adjustable parameters include α_ψ ($= D_\psi/v_\psi$), θ and t_1, which are treated as global fitting parameters (one value per rock), while v_ψ and t_2 are let to vary with flow rate. The TPL model is applied by using a single set of values of α_ψ, β, and t_2 for each rock, while t_1 and v_ψ are let to vary with flow rate. In both cases, parameter fitting has been implemented through a two-step approach: in the first fitting cycle, all parameters are fitted and let vary with experimental flow rate; in the second fitting cycle and for each rock, average values of the global fitting parameters are then used as input to the model, while remaining parameters are fitted to each BTC. We note that for both formulations (SRMT and TPL) the number of fitted parameters is the same, $2\times N_q + 3$, where N_q is the number of flow rates. Values of the fitted parameters are found by minimizing the following objective function:

$$J = \sum_{i=1}^{N_q}\sum_{j=1}^{N_p}\frac{(c_{i,j}^{mod} - c_{i,j}^{exp})^2}{c_{i,max}^{exp}}, \tag{8}$$

where N_q and N_p are the number of flow rates and of experimental points in each BTC; c^{mod} and c^{exp} are the effluent concentration values predicted by the model and measured experimentally, respectively. The denominator in Equation 8 is the maximum value of the measured effluent concentration and ensures uniform weighting of the BTCs. A genetic algorithm was used to solve the optimization problem; to this end, the function `ga` available in the MATLAB global optimization toolbox was used by defining a set of lower and upper bounds on the fitting parameters (Table S4). The population size was fixed at 24 times the number of decision variables, and the number of generations was limited to 100. The relative tolerance on the objective function was set to `TolFun` $= 1\times10^{-7}$.

We note that by imposing a constant dispersivity, α_ψ, in the solution of the optimization problem, we have assumed that the Sheidegger parameterization holds. Using this parameterization, (i) the longitudinal dispersion coefficient does not depend on the value of the diffusion coefficient, and (ii) it scales linearly

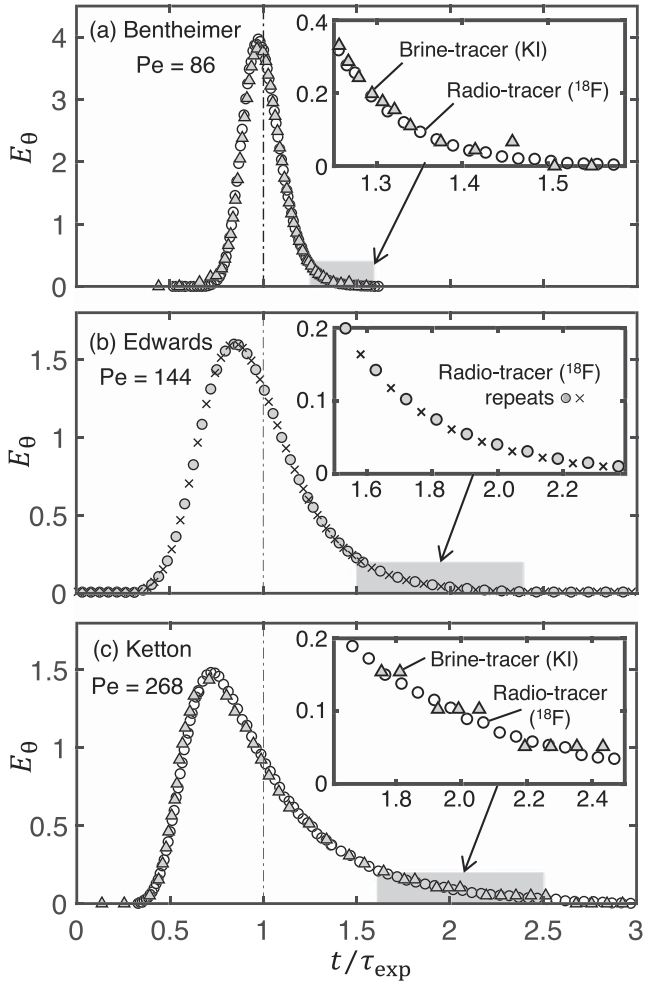

Figure 5. Residence time distribution (RTD) functions, E_Θ, measured on (a) BS, (b) EB, and (c) KL plotted as a function of the reduced time, t/τ_{exp}. For (a) and (c) two sets of BTCs are plotted that have been measured using the brine (KI)- (filled triangles) and radio(^{18}FDG)-tracer (empty circles). For (b), two data sets are plotted that represent a repeat of the same experiment with the radio tracer. The inset in each plot is a close-up of the tail of the measured BTC.

with the mean pore velocity, that is, $D_\psi = \alpha_{\psi v_\psi}$. For the range of Péclet numbers considered in this work ($Pe = vD_e/\mathcal{D} > 10$), advection dominates over diffusion everywhere and (i) is therefore satisfied. Assessing the validity of (ii) is more complex: While the imposed linearity holds for uniform media at sufficiently large Peclet number (see, e.g., data on beadpacks [BPs] reported in Kurotori et al., 2019), it is likely to be invalid for highly heterogeneous media, such as those characterized by strong spatial variation in permeability in the direction of flow or by pronounced mobile and immobile zones. It is one of the aims of this study to verify the applicability of this parameterization for the three rock samples considered.

4. Results

A selection of BTCs measured on the three rock samples is shown in Figure 5 in terms of the normalized Residence Time Distribution (RTD) function, $E_\Theta = \tau_{exp}E(t)$, as a function of the reduced time, t/τ_{exp}. This formulation enables to account for the variation in radio-tracer feed concentration (as a result of radioactive decay between experiments) and to compare between brine and radio-tracer measurements (Kurotori et al., 2019). An excellent agreement is observed between curves measured using the radio and the brine tracers for both BS (Figure 5a) and KL (Figure 5b). For EB (Figure 5c), the plotted curves are repeats of the same experiment with the radio tracer. We note that, in addition to reproducibility, radioactivity provides sufficient measurement sensitivity down to concentration values that are 4 orders of magnitude smaller than the inlet concentration (logarithmic plots of the tracer effluent curves are shown later in Figure 7). For both measurement methods, we have computed the signal-to-noise ratio, SNR, yielding a value for the radio tracer that is about 400 times larger than the one obtained with the brine tracer (details on the calculation described in section S4). As indicated by the close-up of the BTC shown in the inset of Figures 5a and 5b, it can indeed be observed that conductivity measurements loose the required sensitivity at low concentrations for the conditions tested in this study ($c_{F0} = 0.064$ g/ml).

A total of 6, 6, and 10 tracer injections were conducted for BS, EB, and KL, respectively, over the range of flow rates q = 2–19 ml/min. These correspond to Pe = 17–163 (BS), Pe = 19–183 (EB), and Pe = 54–509 (KL), when using the mean equivalent grain diameter as the characteristic length scale for mixing (Table 1). Tables S1 (BS), S2 (EV), and S3 (KL) provide a summary of all the tracer tests, including an account of the amount of tracer recovered in each experiment. Overall, tracer recovery is high, with relative deviations between amount injected and produced that are less than 5% (brine tracer) and 2% (radio tracer) over the range of flow rate studied. Figure 5 also provides a first appraisal of the distinct behavior observed for the three porous materials: BS shows a narrow and symmetric profile centered around the expected mean residence time that is a characteristic of a homogeneous material. On the other hand, results for EB and KL are characterized by an early breakthrough, followed by tailing at late times that continues until about 2–2.5 PVs of fluid have passed through the sample. These are typical features of a condition of nonequilibrium, in which diffusion into and out of intragranular porosity is slow relative to transport driven by advection. Such effects are also seen in the measured value of the mean residence time (τ_{exp}) that deviates systematically from its theoretical counterpart (τ^*) with increasing flow rate for both carbonates (Tables S2 and S3). On the contrary, for the sandstone an excellent agreement is observed at each flow rate between the two values, with deviations less than 0.5% (Table S1).

4.1. Characteristic RTD Functions

The full set of radio-tracer experiments carried out in this study are presented in Figure 6, again in the form of RTD functions. By means of comparison, previously reported observations on a random BP (using a brine

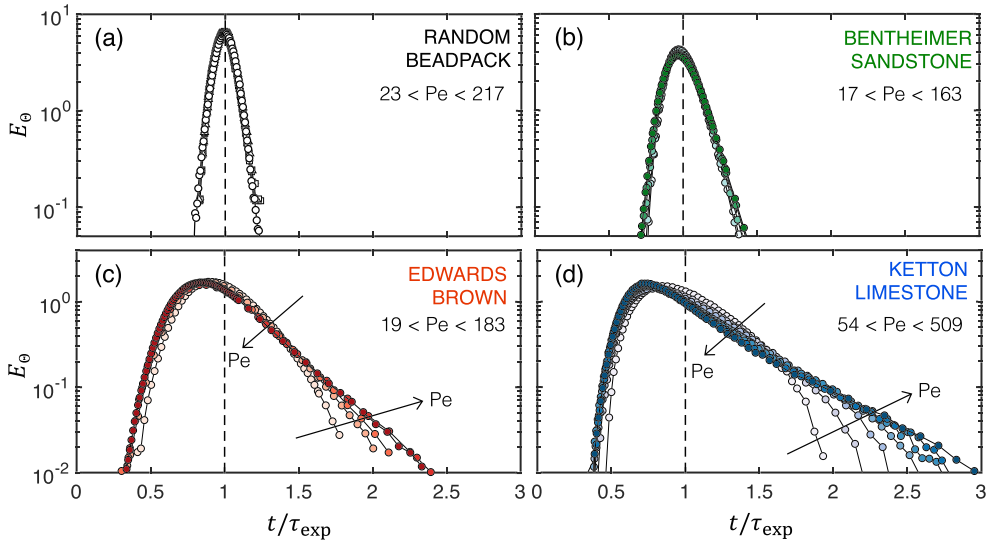

Figure 6. Normalized RTD function, E_Θ, as a function of the reduced time, t/τ_{exp}, for pulse-tracer experiments carried out on (a) random beadpack, (b) Bentheimer Sandstone, (c) Edwards Brown, and (d) Ketton Limestone. For each sample, experiments have been carried out at various flow rates, corresponding to the range of Pe indicated in each plot. Data plotted in (a) and (d) have been published in Kurotori et al. (2019).

tracer) (Kurotori et al., 2019) are also shown in the figure. The width of the measured effluent concentration profiles increases in the order BP < BS < EB < KL, indicating an increase of the nonequilibrium effects anticipated above. The profiles measured on BP are symmetric and centered around the mean residence time ($t/\tau_{exp} = 1$), while a slight deviation is observed for those obtained on BS together with an increase in the width of the RTD ($t/\tau_{exp} \approx 0.7$–1.4). Nevertheless, in both cases the set of measured BTCs (five for BP and six for BS) form a single characteristic curve; this further suggests that over the range of Pe investigated here ($17 \leq Pe \leq 163$), an approach based on the ADE with a constant dispersivity coefficient would be sufficient to capture the observed behavior (see section 5).

The two sets of tracer BTCs measured on the carbonate samples are much more dispersed and indicate a more complex transport process. The RTD functions are characterized by a significant early breakthrough ($t/\tau_{exp} \approx 0.4$), followed by pronounced tailing that continues until about $t/\tau_{exp} \approx 2.5$ (EB) and 3 (KL) at the largest flow rate investigated. Moreover, for both samples the set of measured BTCs no longer gather around a single characteristic curve, but the data diverge at late times with the strength of the tailing that increases with Pe. As anticipated above, these features are most likely the manifestation of nonequilibrium effects arising from distinct transport mechanisms that evolve over different time scales, such as those associated with advection and diffusion. Specifically, both rocks possess a significant fraction of submicron porosity (33% for KL and 10% for EB, as estimated from Figure 2), with EB also showing signs of developed vuggy porosity (Figure 1). These features can be associated with parts of the porous domain that have limited fluid motion and where molecular diffusion cannot homogenise the evolution of the concentration distribution. Under these circumstances, the ADE would fail at matching the resulting experimental BTCs, requiring a model where the presence of these structural features (and the associated transport mechanism) is explicitly taken into account.

4.2. Modeling of the BTCs

The results obtained upon fitting the SRMT (blue lines) and TPL model (red lines) to the experimental BTCs (symbols) measured on BS (top panel), EB (middle panel), and KL (bottom panel) are shown in Figure 7. For the sake of clarity, results are shown only for three flow rates ($q = 4$, 10, and 19 ml/min), and the corresponding parameter values are summarized in Table 2. The data associated with the remaining flow rates, including the graphical comparison between models and experiments, are reported in the supporting information (sections S6 and S7). For each rock sample and each one of the flow rates considered, two plots are shown in Figure 7, namely, the comparison of best model fits with the experimental breakthrough data (bottom plot) and the deviations between predicted and measured concentration values ($\Delta\bar{c}$, top plot) as a function of the reduced time. Overall, the two models provide very good fit to the experimental data over the

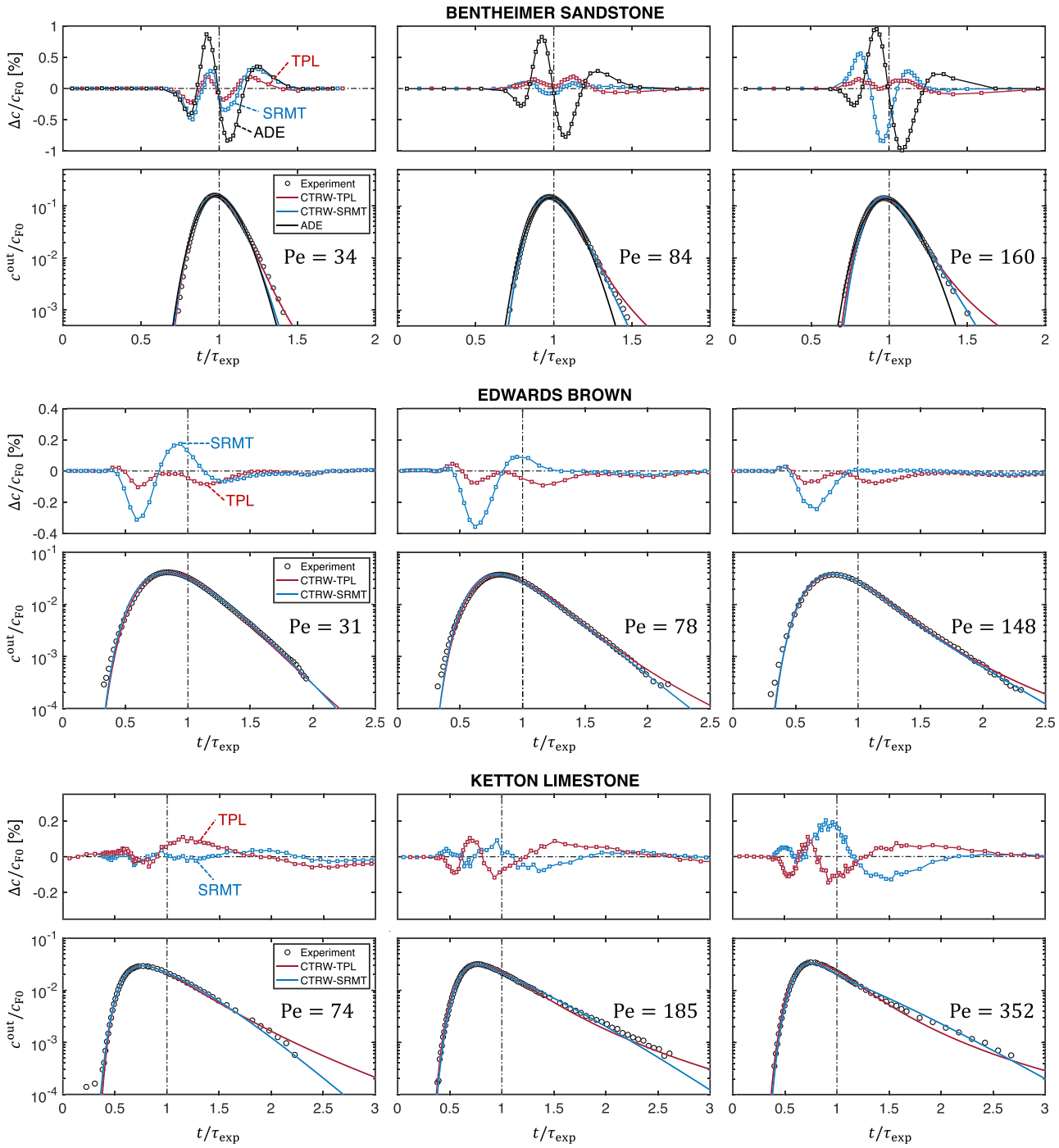

Figure 7. Comparisons of best model fits with the SRMT (blue lines) and TPL (red lines) models in the CTRW formulation for the BTCs measured on BS (top panel), EB (middle panel), and KL (bottom panel). Three different flow rates are presented, namely, $q = 4$ ml/min (left), 10 ml/min (center), and 19 ml/min (right). Experimental data are shown as circles, and results are presented as normalized concentration, c^{out}/c_{F0}. Values of $Pe = vD_e/\mathscr{D}$ are given in each plot. For BS, fits obtained using the ADE are also shown (black lines). Above each BTC plot, the corresponding deviations between predicted and measured concentration values ($\Delta c = c^{exp} - c^{mod}$) are plotted as a function of reduced time, t/τ_{exp}.

Table 2
Values of the Parameters Fitted Upon Application of the SRMT and TPL Models to the Measured Tracer BTCs in the Three Rock Samples, Together With the Value of the Objective Function

			Bentheimer	Edwards Brown	Ketton
SRMT	α_ψ [cm]	G	0.041	0.366	0.197
	θ	G	0.049	0.067	0.382
	$\log_{10}(t_1)$	G	−2.62	−1.69	−1.33
	$\log_{10}(t_2)$		−0.510, −0.608, −0.726	0.388, 0.232, 0.111	0.304, 0.028, −0.185
	v_ψ [cm/min]		0.843, 2.10, 3.98	0.519, 1.33, 2.54	1.14, 2.90, 5.61
	J [−]		0.0247	0.0149	0.00785
TPL	α_ψ [cm]	G	0.022	0.18	0.061
	β	G	1.66	1.41	1.46
	$\log_{10}(t_2)$	G	0.49	0.93	1.24
	$\log_{10}(t_1)$		−2.32, −2.68, −2.87	−1.17, −1.76, −2.13	−0.371, −1.14, −1.64
	v_ψ [cm/min]		1.15, 2.92, 5.58	0.879, 2.52, 5.07	1.14, 3.67, 7.86
	J [-]		0.00678	0.00199	0.00995

Note. Parameters labeled as G are "global" (one value per rock sample), while the others vary with flow rate (q = 4, 10, and 19 ml/min). The unit of t_1 and t_2 is min.

whole Pe range, with deviations that are less than 0.2–0.5% between predicted and measured concentration values. Similarly, the difference between the measured and computed mean arrival time of the BTC is less than 1.5% for both models and for each flow rate. Nevertheless, the TPL model shows the best overall fit to the experimental data, as quantified from the smaller values of the objective function (Table 2).

For BS, we have also assessed the application of the ADE (plotted as black line), obtaining satisfactory agreement, albeit with larger deviations (up to 1%). The latter indicate a systematic pattern that includes underprediction at early and late times and overprediction at intermediate times. Similar differences have been reported for other "homogeneous" samples, such as Berea Sandstone (Berkowitz et al., 2006), and are likely due to subtle effects of pore-scale disorder that becomes evident in experiments with relatively short samples ($\mathcal{O}(L) \sim 10$ cm). Similar conclusions can be drawn with regard to the application of the SRMT and TPL models to the experimental data on the two carbonate samples. Again, the TPL model shows the best fits, with deviations that are generally below 0.1%, while slightly larger values are observed with the SRMT model (0.1–0.2%). It is interesting to note that TPL performs significantly better on EB, while the SRMT and TPL fits on KL are essentially equivalent. In the latter case, the conditions for the "immobile-mobile" SRMT model are largely met, because of the substantial fraction of intragranular porosity present in this rock that enables a clear separation between the two domains. It is worth noting that this is, to our knowledge, the first application of the CTRW model to BTCs measured on laboratory carbonate core samples.

In Table 2 the values of the parameters obtained upon fitting the numerical solutions of the SRMT and TPL models to the experimental BTCs shown in Figure 7 (the entire data set is summarized in Tables S5–S7 for the SRMT model and Tables S8–S10 for the TPL model) are summarized. We reiterate that fits were obtained by using a single set of (global) parameters for each rock, namely, $[\alpha_\psi, \theta, t_1]$ (SRMT) and $[\alpha_\psi, \beta, t_2]$ (TPL). Accordingly, for each rock the ratio of D_ψ/v_ψ was kept constant, with the changes in v_ψ corresponding to changes in the flow rate. Interestingly, both models predict similar trends for the dispersivity coefficient, which increases in the order BS < KL < EB, reflecting an increase in the medium heterogeneity. The latter is also quantified by the value of β that is used in the TPL model to describe the distribution of transit times and that decreases in the order BS > KL > EB. We note that the value obtained for BS ($\beta = 1.66$) is similar to estimates reported on Berea Sandstone ($\beta = 1.59$) (Cortis & Berkowitz, 2004) and other homogeneous systems, such as sandpacks ($\beta = 1.66$) (Berkowitz & Scher, 2009). Another important parameter of the TPL formulation is the so-called cutoff time, t_2; as expected, for the three rocks tested $t_2 >> t_1$, but its value increases in a different order BS (3.1 min) < EB (8.5 min) < KL (17.4 min).

For BS and over the range of flow rates tested, the mean residence times occur at $\tau_{exp} \approx 2.8$–26 min, and the times for the BTCs to reach $c/c_{F0} \approx 0$ are ≈4–40 min; accordingly, transport has evolved to fully Fickian by the time the tracer breaks through, in agreement with the considerations above on the suitability

of the ADE. On the contrary, for both carbonates samples, this transition has not occurred, despite the time scale for the experiment generally extends beyond the cutoff time. For EB, $\tau_{exp} \approx 4.5$–44 min, and $c/c_{F0} \approx 0$ is reached at ≈10–80 min. For KL, $\tau_{exp} \approx 2.4$–24 min, and $c/c_{F0} \approx 0$ is reached at ≈10–60 min. The persistence of such anomalous behavior may be attributed to mass transport limitations into and out of relatively stagnant regions, which in the carbonate rocks are represented by domains characterized by submicron porosity and vugs. The values for θ obtained from the SRMT model fits provide for some additional insight. For KL $\theta = 0.382$, corresponding to a mobile porosity $\phi = 0.17$ ($\phi/\phi_t = 0.72$), indicating that the long-time tailing observed in the BTCs is indeed largely controlled by the presence of microporosity. For EB $\theta = 0.067$ (corresponding to $\phi = 0.38$ and $\phi/\phi_t = 0.94$), suggesting that subcore permeability heterogeneity may be the dominant "first-order" mass transfer mechanism (also referred to as "advective trapping"; Berkowitz et al., 2006). Notably, these estimates are largely aligned with the results from the independent measurements reported in section 2.2.

5. Discussion

Solute transport in laboratory rock cores is significantly effected by the presence of small-scale heterogeneities, giving rise to BTCs that exhibit anomalous features, such as early breakthrough and long-time tailing. Formulations based on the ADE and the MRMT approach are commonly deployed to interpret these laboratory-scale analyses. Issues of parameters fitting and their interpretation may arise, when these transport theories are not correctly evaluated in the context of the given problem. Additional issues are encountered when the approach to data interpretation relies on the independent evaluation of single BTC experiments, thereby yielding parameters that may show no consistent relationship with experimental variables, such as the flow rate (Berkowitz & Scher, 2009; Khan & Jury, 1990). For the widely studied Berea Sandstone, the range of longitudinal dispersivity values reported in the literature varies by 1 order of magnitude ($\alpha_L = 0.04$–0.4 cm, as summarized in Pini & Krevor, 2019), depending on the model formulation (ADE or MRMT). For the oolitic KL, another well-sorted rock, large variations have been observed in both the longitudinal dispersivity ($\alpha_L = 0.05$–0.16 cm) and the fraction of the pore-space that is considered stagnant ($\phi_{mi}/\phi_t = 0$–0.3), within the same experimental data set (Honari et al., 2015).

In this study, we have presented results from an extensive experimental campaign involving a total of 22 pulse-tracer tests with three laboratory rock cores with distinct pore structures, namely, BS, EB carbonate, and KL. We have adopted the CTRW formalism to interpret the measured BTCs by using distinct expressions for the underlying memory function. Specifically, the distribution of transition times was described using the TPL and with a pdf that exactly represents a first-order, single-rate mass transfer process between mobile and (pseudo)immobile zones (SRMT). The physical basis for the latter is the presence of a substantial fraction of intragranular microporosity in carbonate rocks or, more generally, of domains with significantly different fluid mobility. The resulting retardation with respect to solutes that do not access these domains gives rise to anomalous transport behavior. The TPL takes a more general interpretation of anomalous transport by considering a hierarchy of length scales that ultimately determines the relative strength of advective and diffusive processes.

When compared to the ADE, the CTRW formalism requires more parameters to describe a BTC, and its application may introduce additional uncertainties in the obtained transport coefficients. In our approach to the modeling, we have successfully used BTCs measured at different flow rates to better constrain the fitting of the CTRW model parameters and to identify those that are solely rock dependent (referred to as global parameters). The resulting optimization problem uses the same number of adjustable parameters for the TPL and SMRT models, enabling a direct comparison of their performance. Overall, a better fit of the experimental BTCs was obtained with the TPL model, yielding either comparable (KL) or smaller values of the objective function (BS and EB) than those obtained using the SMRT model. Nevertheless, the observed ability of both models to capture the experimental observations over a range of heterogeneity and time scales is compelling and provides additional confirmation for their suitability in describing chemical transport in rocks. The ability to relate the basic parameters of the memory function to the physical properties of the rock samples underpins the predictive ability of the CTRW approach. In the following, we expand on the interpretation of the key parameters of the two formulations (TPL and SRMT). It will become apparent that the two approaches provide consistent yet complementary insight into the transport properties of rocks and on the nature of anomalous transport in carbonates.

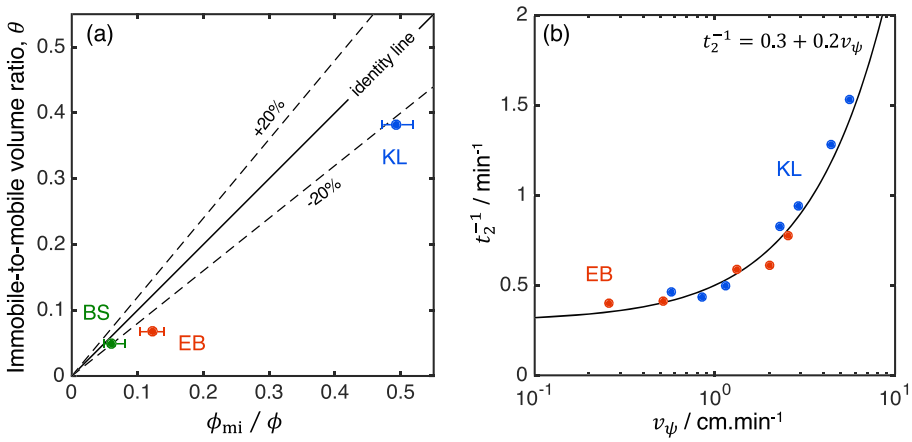

Figure 8. The relevant parameters of the SRMT memory function in the CTRW formulation: (a) volume ratio between immobile to mobile pore space, θ, plotted against the volume fraction of submicron pores obtained experimentally (section 2.2). (b) Estimates of the release time, t_2, for EB (red symbols) and KL (blue symbols) plotted as a function of the particle velocity, v_ψ. The solid line is a linear fit to the data.

5.1. Nonequilibrium Effects in Carbonate Rocks

The SRMT model, Equation 4, assumes randomly distributed regions of different permeability and that the mass exchange between mobile and (pseudo)immobile regions is purely diffusive. A first-order mass transfer model is used to describe this trapping process, by assuming that each immobile zone is fully mixed (uniform concentration). There are three relevant parameters in the conceptualization of this model, namely, the volume ratio between immobile to mobile pore space, θ, and two time domains—the time spent in the mobile phase (t_1) and the release time from the traps (t_2). In Figure 8a the values of θ for the three rocks obtained by fitting against those obtained from independent experimental observations are plotted (section 2.2). Overall, there is a very good agreement between the two sets of data, with θ increasing in the order BS < EB < KL. We note that in the CTRW model the value of θ is constant; as such we have not used concepts such as "effective porosity" (Honari et al., 2015) to introduce an apparent dependency of the fraction of the mobile pore space on the flow rate.

In our fitting of the experimental data, we have observed that among the two characteristic time domains, t_2 largely dominates the transport and that t_1 has a very weak effect. Accordingly, we have set t_1 as global fitting parameter and let t_2 to depend on the velocity. Estimates of the release time, t_2, for the two carbonate samples are shown Figure 8b as a function of the particle velocity, v_ψ, and are also summarized in Tables S6 and S7. It can be seen that for both rocks, t_2^{-1} increases with v_ψ, yielding a single characteristic curve that is well described by a linear correlation, $t_2^{-1} = 0.3 + 0.2 \times v_\psi$. The rate dependency of the mass exchange term is not surprising given that a single-rate mass transfer process has been assumed that lumps together different mass transfer processes that may take place over distinct characteristic times. While the velocity dependence of t_2 in the SRMT model may be debatable, it was needed to obtain a satisfactory fit to the experimental data. In this context, some authors have assumed that the single-rate mass transfer coefficient ($\propto t_2$) varies with time (Fernàndez-Garcia & Sanchez-Vila, 2015). Others have adopted a formulation where the concentration "seen" by the immobile regions depends on the fluid velocity and differs from the bulk or average concentration in the mobile region (Municchi & Icardi, 2020). We note that Equation 4 could in principle be used to explicitly describe diffusive transport within the immobile zone, in a formulation that mimics a multirate mass transport process, albeit with an increase of the number of fitting parameters. The good agreement with the experimental observations indicates that the use of one single first-order exchange term is sufficient to capture the transport process in the carbonate sample and under the conditions investigated in this study.

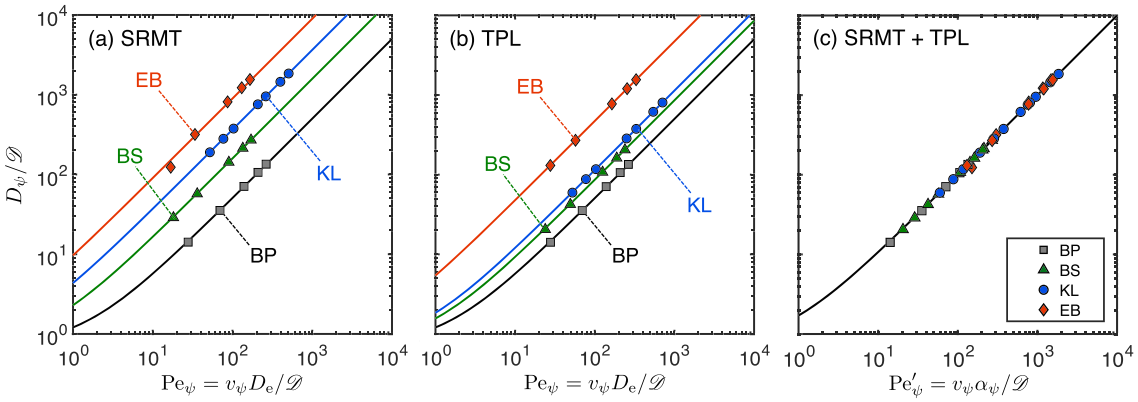

Figure 9. Normalized longitudinal dispersion coefficient ($D_\psi/\mathscr{D}$) plotted as a function of the Péclet number ($\mathrm{Pe}_\psi = v_\psi D_e/\mathscr{D}$) for the results obtained with the (a) SRMT and (b) TPL models. Symbols are experimental data obtained in this work on the rock samples BS (triangles), EB (diamonds), and KL (circles). Data measured on a cylindrical random beadpack in Kurotori et al. (2019) are also shown (BP, squares). In (c) the same data as in (a) and (b) are shown but where α_ψ is used as a characteristic length scale in the definition of the Péclet number. In the plots, the solid lines are predictions from an empirical correlation of the form of Equation 9 that uses a inhomogeneity factor, σ_ψ, to scale data measured on different porous media (values reported in Table 3).

5.2. The Characteristic Length Scale of Mixing

Experimental results of hydrodynamic dispersion coefficients of porous media are traditionally presented in a $D_L/\mathscr{D}$ versus $\mathrm{Pe} = vD_e/\mathscr{D}$ plot (Dullien, 1992). The same approach is adopted here by considering the corresponding dimensionless groups in the CTRW formulation, namely, $D_\psi/\mathscr{D}$ and Pe_ψ, for both the SRMT (Figure 9a) and TPL model (Figure 9b). All values are also reported in Tables S5–S7 (SRMT) and Tables S8–S10 (TPL). As anticipated in Berkowitz et al. (2006), we also find here that $v_\psi > v$ (and, accordingly, $\mathrm{Pe}_\psi > \mathrm{Pe}$), where v_ψ represents the average particle velocity, which differs from the average fluid velocity v, when $\tilde{M} \neq 1$. Moreover, for both models we note that the magnitude of the dispersion coefficient increases from BP (data measured in Kurotori et al., 2019), to sandstone (BS) and to the carbonate samples (with KL < EB). For the three samples investigated in this study, the observed trend reflects the increase in complexity of the rock's fabric visible from the microCT tomograms shown in Figure 1. As anticipated in section 3, for each rock a constant value for the dispersivity, α_ψ, was imposed for fitting BTCs measured at different flow rates, implying that $D_\psi/\mathscr{D} \propto \mathrm{Pe}_\psi$. This behavior is verified in Figures 9a and 9b by plotting alongside the experimental data predictions using a correlation of the following form (Sahimi et al., 1986):

$$\frac{D_L}{\mathscr{D}} = \frac{1}{\sqrt{2}} + 0.5\sigma \mathrm{Pe}^m, \tag{9}$$

where m has been set to 1 (the Sheidegger parameterization). The coefficient σ has been previously referred to as the "inhomogeneity" factor (Perkins & Johnston, 1963) to quantify any departure from a homogeneous system ($\sigma = 1$ for the random BP, while $\sigma > 1$ for more heterogeneous systems). Here, we have successfully extended the applicability of this correlation to data obtained upon application of the CTRW formalism (and by using in Equation 9 the parameters σ_ψ, D_ψ, and Pe_ψ). It can be readily shown that $\sigma_\psi = 2\alpha_\psi/D_e$; this measure provides therefore a direct link between a characteristic microscopic length-scale of the rock (D_e) and the characteristic length-scale for transport (α_ψ).

The obtained values are summarized in Table 3 and indicate that for both models the obtained inhomogeneity factor increases in the order BS < KL < EB. Notably, the inhomogeneity factors are well above a value of 1, further indicating that for the three rocks the dispersivity $\alpha_\psi > 1 \times D_e$, reaching values up to $\approx 5 - 10 \times D_e$ for the vugular carbonate (EB). For reference, we note that for a homogeneous porous medium (similar to the random BP in Figure 9), Random-Walk simulations indicate that $\alpha_L = \alpha_\psi = 0.5 \times D_e$ (Gist et al., 1990). When the dispersivity is used as the characteristic length scale in the definition of the Péclet number ($\mathrm{Pe}' = v_\psi \alpha_\psi/\mathscr{D}$), all data are expected to gather into a single universal curve. This result is demonstrated in Figure 9c for both TPL and SMRT models. This observation is of particular significance, because it provides experimental evidence that the transport parameters of the rocks investigated are well captured using a fairly simple description of the mixing process that imposes the Sheidegger approximation, despite the obvious differences in both their pore structure and textural parameters.

Table 3
Heterogeneity Measures for the Three Rocks Investigated in This Study

	Bentheimer	Edwards Brown	Ketton
$\sigma_\psi/2$ (SRMT)	1.6	9.4	3.6
$\sigma_\psi/2$ (TPL)	0.9	4.7	1.1
l/D_e	2.4	2.6	2.7
$\bar{d}/D_e$	0.3	1.1	6.1

Note. σ_ψ is the inhomogeneity factor and is defined as twice the ratio of dispersivity (α_ψ) to mean grain diameter, D_e; l is the heterogeneity length scale associated with the t_2 value in the TPL model, while $\bar{d}$ is associated with t_1 and represents the characteristic length for particle transitions between sites.

5.3. The Characteristic Heterogeneity Length-Scale

As discussed in section 4.2, the BTCs measured on the three rocks were well matched by the CTRW model that uses a TPL for the time function $\psi(t)$. In our approach to the modeling, the latter was constrained to a single set of the parameters β and t_2 for each rock, while letting t_1 to vary with flow rate. The resulting $\psi(t)$ functions for the three rocks are shown in Figure 10 for $\mathrm{Pe}_\psi \approx 55$. As discussed in Dentz et al. (2004), $\psi(t) \propto (t/t_1)^{-(1+\beta)}$ for $t_1 \ll t \ll t_2$; our data suggest that this power law dependence of travel times is well captured for the three rocks with $\beta \approx 1.5$. The slight variation among the obtained values of β for the three rocks (see Table 2) is thus an indication of a similar degree of (moderate) heterogeneity. Larger variations are observed for the value of t_2 with the latter increasing in the order BS < EB < KL (see Table 2 and the inset in Figure 10). Notably, when the dimensionless time $\tilde{\tau}$ ($\equiv t/t_1$) is considered (main plot), this order is reversed, and the region when the power law dependency of travel times is observed ($1 \ll \tilde{\tau} \ll \tilde{\tau}_2$) becomes shorter for the carbonates. In other words, in carbonates heterogeneities can increase the overall strength of mixing, thereby effectively homogenizing the transport process. We anticipate that more quantitative insight into this mixing process could be obtained from the simultaneous application of noninvasive methods to the study of transport in rocks (Kurotori et al., 2019; Zahasky et al., 2019).

As indicated in Dentz et al. (2004), t_2 can be associated to the largest heterogeneity length scale l in the porous medium, and, accordingly, transport on a scale $L \gg l$ is expected to evolve to Fickian, if the transport processes lead to fully mixed conditions over the length scale l (remind that $t_1 < t_2$). In this context, t_2 can also be interpreted as the time to diffuse over the length scale l, that is, $t_2 = l^2/2\mathscr{D}$ (Bijeljic & Blunt, 2006), where $\mathscr{D} = 1\times10^{-5}$ cm^2/s is the bulk molecular coefficient in the liquid. For the three rocks investigated in this study, we obtain $l = 0.6$ mm (BS), 1.0 mm (EB), and 1.4 mm (KL), showing an increase from the rather homogeneous sandstone to the texturally more complex carbonates. We note however that for the three rocks $l/D_e \approx 2.5$ (values reported in Table 3); that is, the increase is only apparent, and it disappears when the mean equivalent grain size D_e of each rock is considered. This observation agrees with the observed weak variation discussed above of the parameter β, which also serves as a measure for the strength of heterogeneity. Another important length scale of the TPL model is associated with the advection process; recalling that t_1 represents a median transition time (section 3.1), one can define $t_1 = \bar{d}/v_\psi$, where $\bar{d}$ is the characteristic length for the transition. As shown in Figure 11, the latter can be readily obtained from a plot of the transition time as a function of $1/v_\psi$. In the plot, the dashed lines represent linear fits to the data, corresponding to values of $\bar{d} = 0.066$ mm (BS), 0.43 mm (EB), and 3.3 mm (KL). In agreement with previous observations on homogeneous and heterogeneous sandpacks (Berkowitz & Scher, 2009), we observe here that the advective length scale is constant over the range of flow velocities considered in this study. The value of $\bar{d}$ for BS is found to be significantly smaller than the equivalent diameter of the rock ($\bar{d}/D_e \approx 0.26$), while the ratio increases well above one for the carbonates, namely, $\bar{d}/D_e \approx 1.1$ for EB

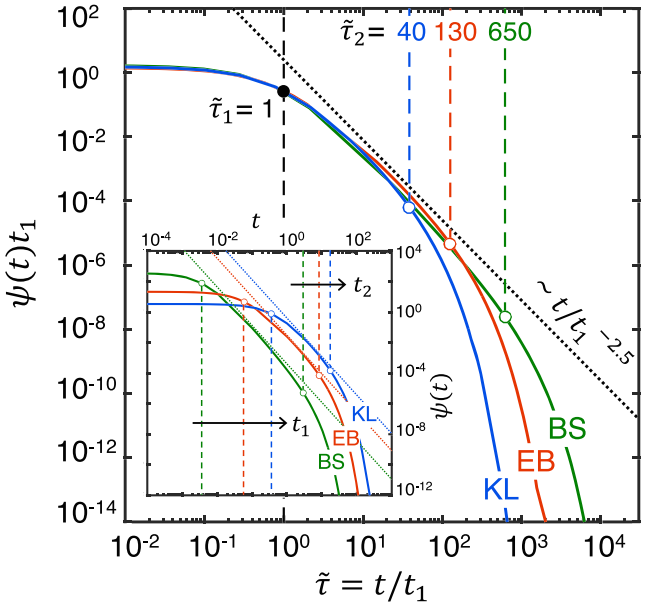

Figure 10. Behavior of the TPL $\psi(t)$ in the CTRW model for the three rocks investigated in this study. The curves are shown for $\mathrm{Pe}_\psi \approx 55$ and the following values for the set of parameters [$\log_{10}(t_1)$, $\log_{10}(t_2)$, β]: BS [−2.325, 0.49, 1.66], EB [−1.17, 0.93, 1.41], and KL [−0.341, 1.24, 1.46]. The dotted line indicates the power law behavior $\psi(t) \propto (t/t_1)^{-(1+\beta)}$.

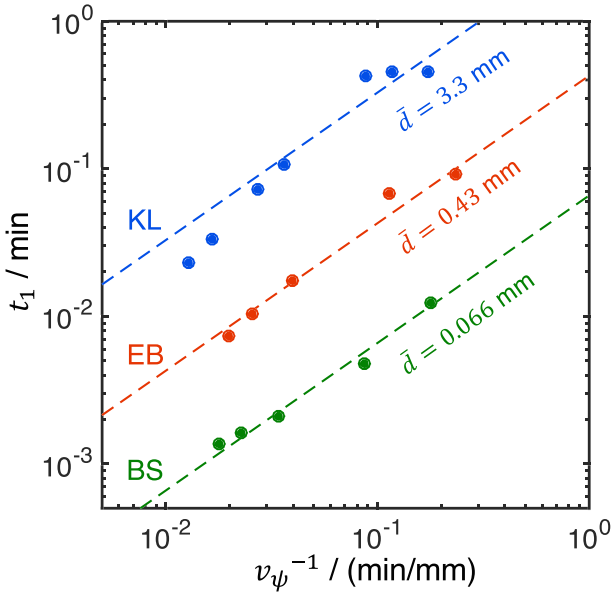

Figure 11. Median transition time, t_1, as a function of the reciprocal velocity, $1/v_\psi$, as obtained from fitting the CTRW model to the tracer BTCs measured on the three rocks. Dashed lines are straight lines fitted to the data and passing through the origin, $t_1 = \bar{d}/v_\psi$.

and $\bar{d}/D_e \approx 6.1$ for KL. The analysis of the ratio $l/\bar{d}$ provides for additional insight. For BS $l/\bar{d} \approx 9 \gg 1$, indicating that the fairly regular porous structure of this sandstone enables probing a sufficiently large PV for the transport to be largely Fickian at the experimental conditions investigated here. On the contrary, $l/\bar{d} \approx 0.4 < 1$ for the microporous KL, reflecting a situation of anomalous transport, where diffusion cannot keep up with advection and rapidly changing concentrations. With $l/\bar{d} \approx 2.4$, EB lies between these two cases, as a result of moderate microporosity and stronger textural heterogeneity compared to the sandstone. Notably, the data shown in Figure 11 for KL also indicate a deviation from a unique linear dependency at large flow rates ($v_\psi > 10$ mm/min) toward larger values for $\bar{d}$; we (again) attribute this result to the presence of intragranular microporosity in this limestone that introduces significant mass transfer limitations between parts of the domain where advection dominates versus where water is relatively stagnant.

6. Concluding Remarks

The description of chemical transport in rocks requires understanding their multiscale heterogeneities and their effects on the mixing process. The current data set reported in the literature for the transport properties of laboratory rock samples is still very limited, particularly for carbonates, and the obtained transport coefficients are largely scattered. Major drivers for this variability have been (i) the lack of observations over a wide range of flow rates (or Pe) and (ii) the uncertainty associated with the selection of a suitable transport model. In this study, we have applied the CTRW formulation to a comprehensive set of unidirectional tracer tests carried out using three rock cores with different pore structures. In addition to the TPL, two different expressions of the underlying memory function were evaluated to also consider classic formulations based on ADE and single-rate mass transfer between mobile and immobile domains (SRMT). Relative to most analyses presented in the literature, we have used observations over a wide range of flow rates ($10 < \mathcal{O}(\mathrm{Pe}) < 100$) to identify fitting parameters that are solely rock dependent. In this effort, we have also probed the operating envelope of the CTRW formalism, whose application at the lab scale has been so far limited to model systems (e.g., sandpacks) or model rocks, such as Berea Sandstone.

Both the TPL and SRMT models, formulated with the Sheidegger approximation ($D_L \propto \mathrm{Pe}$), provide excellent fits to the experimental data on the three rocks. The two models offer consistent insight on the obtained transport properties, as revealed through the observed trends in their characteristic parameters (e.g., the longitudinal dispersivity) and the comparison against independent observations from textural analysis. The two models also offer a mechanistic view into the underlying transport processes, which in carbonate rocks may evolve over different time scales, namely, (i) advection and (ii) diffusion into and out of relatively stagnant regions. In the SRMT model, the rate of mass transfer between the flowing fluid and the porous grains is linearly proportional to the velocity and is universal to both carbonate samples. In the TPL model, the interplay between the two transport processes was described through the ratio of their characteristic length scales, which can be estimated from the characteristic transit times of the underlying memory function (t_1(Pe) and t_2). Such systematic comparison of two important transport models is thus not only highly instructive but provides complementary insight on the nature of anomalous transport in laboratory rock samples.

Notation

A	sample cross section
$A_{g,e}$	equivalent grain surface ($= \pi D_e^2$)
c	tracer concentration ($\tilde{c} = \mathcal{L}\{c\}$)
c_{F0}	tracer feed concentration
c^{out}	effluent concentration ($= c(z = L, t)$)
D_e	mean equivalent grain diameter
$d_{e,j}$	equivalent diameter of grain class j ($= (6V_{g,j}/\pi)^{1/3}$)
$\bar{d}$	characteristic transition length (CTRW-TPL model; $= t_1 v_\psi$)

$\mathscr{D}$	molecular diffusion coefficient
D_L	longitudinal dispersion coefficient
D_ψ	"dispersion coefficient" (CTRW formulation)
$E(t)$	Residence Time Distribution (RTD) function ($= c^{out}/\int_0^\infty c^{out}dt$)
$E_\Theta(t)$	normalized RTD function ($= \tau_{exp}E(t)$)
K	permeability
l	characteristic heterogeneity length scale (CTRW-TPL model)
J	objective function
L	sample length
M	memory function (CTRW formulation; $\tilde{M} = \mathcal{L}\{M\}$)
Pe	Peclet number ($= vD_e/\mathscr{D}$)
Pe_ψ	Peclet number ($= v_\psi D_e/\mathscr{D}$, CTRW formulation)
q	volumetric flow rate ($=uA$)
R_p	mean pore-throat radius
s	Laplace variable
t	time
t_1	median particle transition time (CTRW formulation, $= \bar{d}/v_\psi$)
t_2	cutoff time ($= l^2/(2\mathscr{D})$, CTRW-TPM) or release time from traps (CTRW-SRMT)
u	superficial velocity
v	interstitial velocity ($=u/\phi$)
v_ψ	mean particle velocity (CTRW formulation)
V_g	grain volume
x	dimensionless spatial coordinate ($=z/D_e$)
z	spatial coordinate

Greek Letters

α_L	longitudinal dispersivity ($= D_L/v$)
α_ψ	"dispersivity" (CTRW model, $= D_\psi/v_\psi$)
β	parameter of the $\psi(t)$ function
θ	immobile-to-mobile pore volume ratio (CTRW-SRMT model)
ϵ	duration of square input function
ϕ	intergranular (mobile) porosity
ϕ_{mi}	intragranular porosity
ϕ_t	total porosity ($= \phi + \phi_{mi}$)
ρ_{sk}	skeletal density
ρ_b	bulk density
σ	inhomogeneity factor ($= 2\alpha/D_e$)
σ_{psi}	inhomogeneity factor ($= 2\alpha_\psi/D_e$, CTRW formulation)
σ_{std}	standard deviation
τ	dimensionless time ($= t\mathscr{D}/D_e^2$)
$\tilde{\tau}$	reduced time ($=t/t_1$)
τ_{exp}	mean residence time ($= \int_0^\infty tE(t)dt$)
$\tau*$	average residence time ($= L/v$)
$\psi(t)$	PDF of transit times (CTRW formulation; $\tilde{\psi} = \mathcal{L}\{\psi\}$)
Ψ	sphericity ($= \pi^{1/3}(6V_g)^{2/3}/A_g$)

Acknowledgments
This work was carried out as part of the Qatar Carbonates and Carbon Storage Centre (QCCSRC). The authors gratefully acknowledge the funding of QCCSRC provided jointly by Qatar Petroleum, Shell, and the Qatar Science and Technology Park. Saurabh M. Shah is acknowledged for his assistance in acquiring the micro-CT images. Radio-tracer experiments and funding were also provided by the Global Climate Energy Project at Stanford University.

Data Availability Statement

The experimental tracer curves associated with this work may be obtained from the Imperial College London Research Data repository using the following: https://doi.org/10.14469/hpc/6943 (embargoed until paper acceptance).

References

Berkowitz, B., Cortis, A., Dentz, M., & Scher, H. (2006). Modeling non-Fickian transport in geological formations as a continuous time random walk. *Reviews of Geophysics*, *44*(2), RG2003. https://doi.org/10.1029/2005RG000178

Berkowitz, B., & Scher, H. (2009). Exploring the nature of non-Fickian transport in laboratory experiments. *Advances in Water Resources*, *32*(5), 750–755.

Bijeljic, B., & Blunt, M. J. (2006). Pore-scale modeling and continuous time random walk analysis of dispersion in porous media. *Water Resources Research*, *42*, W01202. https://doi.org/10.1029/2005WR004578

Bijeljic, B., Mostaghimi, P., & Blunt, M. J. (2011). Signature of non-Fickian solute transport in complex heterogeneous porous media. *Physical Review Letters*, *107*(20), 204,502.

Bijeljic, B., Mostaghimi, P., & Blunt, M. J. (2013). Insights into non-Fickian solute transport in carbonates. *Water Resources Research*, *49*, 2714–2728. https://doi.org/10.1002/wrcr.20238

Bijeljic, B., Muggeridge, A. H., & Blunt, M. J. (2004). Pore-scale modeling of longitudinal dispersion. *Water Resources Research*, *40*, W11501. https://doi.org/10.1029/2004WR003567

Bretz, R. E., & Orr, F. M. (1987). Interpretation of miscible displacements in laboratory cores. *SPE Reservoir Engineering*, *2*(04), 492–500.

Carrera, J., Sánchez-Vila, X., Benet, I., Medina, A., Galarza, G., & Guimerà, J. (1998). On matrix diffusion: Formulations, solution methods and qualitative effects. *Hydrogeology Journal*, *6*(1), 178–190.

Coats, K., Smith, B., van Genuchten, M. T., & Wierenga, P. J. (1964). Dead-end pore volume and dispersion in porous media. *Society of Petroleum Engineers Journal*, *4*(01), 73–84.

Cortis, A., & Berkowitz, B. (2004). Anomalous transport in "classical" soil and sand columns. *Soil Science Society of America Journal*, *68*(5), 1539–1548.

Cortis, A., & Berkowitz, B. (2005). Computing "anomalous" contaminant transport in porous media: The CTRW MATLAB Toolbox. *Ground Water*, *43*(6), 947–950.

Dentz, M., & Berkowitz, B. (2003). Transport behavior of a passive solute in continuous time random walks and multirate mass transfer. *Water Resources Research*, *39*(5), 1111. https://doi.org/10.1029/2001WR001163

Dentz, M., Cortis, A., Scher, H., & Berkowitz, B. (2004). Time behavior of solute transport in heterogeneous media: Transition from anomalous to normal transport. *Advances in Water Resources*, *27*(2), 155–173.

Dentz, M., Le Borgne, T., Englert, A., & Bijeljic, B. (2011). Mixing, spreading and reaction in heterogeneous media: A brief review. *Journal of Contaminant Hydrology*, *120-121*, 1–17.

Dullien, F. (1992). *Porous media: Fluid transport and pore structure*. London: Academic Press, Inc.

Fernàndez-Garcia, D., & Sanchez-Vila, X. (2015). Mathematical equivalence between time-dependent single-rate and multirate mass transfer models. *Water Resources Research*, *51*, 3166–3180. https://doi.org/10.1002/2014WR016348

Fogler, H. S. (1999). *Elements of chemical reaction engineering*. Upper Saddle River, NJ: Prentice Hall PTR.

Gist, G. A., Thompson, A. H., Katz, A. J., & Higgins, R. L. (1990). Hydrodynamic dispersion and pore geometry in consolidated rock. *Physics of Fluids A: Fluid Dynamics*, *2*(9), 1533–1544.

Grattoni, C., Bidner, M., Rosen, M., & Chertcoff, R. (1987). Use of radioisotopes to measure concentration distributions inside porous media during displacement tests. *Chemical engineering science*, *42*(8), 2055–2059.

Haggerty, R., & Gorelick, S. M. (1995). Multiple rate mass transfer for modeling diffusion and surface reactions in media with pore-scale heterogeneity. *Water Resources Research*, *31*(10), 2383–2400.

Haggerty, R., McKenna, S. A., & Meigs, L. C. (2000). On the late-time behavior of tracer test breakthrough curves. *Water Resources Research*, *36*(12), 3467–3479.

Honari, A., Bijeljic, B., Johns, M. L., & May, E. F. (2015). Enhanced gas recovery with CO_2 sequestration: The effect of medium heterogeneity on the dispersion of supercritical CH_4-CO_2. *International Journal of Greenhouse Gas Control*, *39*, 39–50.

Khan, A. U. H., & Jury, W. A. (1990). A laboratory study of the dispersion scale effect in column outflow experiments. *Journal of Contaminant Hydrology*, *5*(2), 119–131.

Kitanidis, P. (2017). Teaching and communicating dispersion in hydrogeology, with emphasis on the applicability of the Fickian model. *Advances in water resources*, *106*, 11–23.

Kurotori, T., Zahasky, C., Hosseinzadeh Hejazi, S. A., Shah, S. M., Benson, S. M., & Pini, R. (2019). Measuring, imaging and modelling solute transport in a microporous limestone. *Chemical Engineering Science*, *196*, 366–383.

Le Borgne, T., Dentz, M., Davy, P., Bolster, D., Carrera, J., de Dreuzy, J. R., & Bour, O. (2011). Persistence of incomplete mixing: A key to anomalous transport. *Physical Review E*, *84*(1), 15,301.

Municchi, F., & Icardi, M. (2020). Generalized multirate models for conjugate transfer in heterogeneous materials. *Physical Review Research*, *2*(1), 013,041.

Neuman, S. P., & Tartakovsky, D. M. (2009). Perspective on theories of non-Fickian transport in heterogeneous media. *Advances in Water Resources*, *32*(5), 670–680.

Perkins, T., & Johnston, O. (1963). A review of diffusion and dispersion in porous media. *Society of Petroleum Engineers Journal*, *3*(01), 70–84.

Pini, R., & Krevor, S. (2019). Laboratory studies to understand the controls on flow and transport for CO_2 storage. In P. Newell & A. G. Ilgen (Eds.), *Science of Carbon Storage in Deep Saline Formations* (pp. 145–180). Oxford, United Kingdom: Elsevier.

Pini, R., Vandehey, N. T., Druhan, J., O'Neil, J. P., & Benson, S. M. (2016). Quantifying solute spreading and mixing in reservoir rocks using 3-D PET imaging. *Journal of Fluid Mechanics*, *796*, 558–587.

Ringrose, P., Sorbie, K., Corbett, P., & Jensen, J. (1993). Immiscible flow behaviour in laminated and cross-bedded sandstones. *Journal of Petroleum Science and Engineering*, *9*(2), 103–124.

Sahimi, M., Hughes, B. D., Scriven, L. E., & Davis, H. T. (1986). Dispersion in flow through porous media—I. One-phase flow. *Chemical Engineering Science*, *41*(8), 2103–2122.

Silliman, S. E., & Simpson, E. S. (1987). Laboratory evidence of the scale effect in dispersion of solutes in porous media. *Water Resources Research*, *23*(8), 1667–1673.

Steefel, C. I., & Maher, K. (2009). Fluid-rock interaction: A reactive transport approach. *Reviews in mineralogy and geochemistry*, *70*(1), 485–532.

Walsh, M., & Withjack, E. (1994). On some remarkable observations of laboratory dispersion using computed tomography (CT). *Journal of Canadian Petroleum Technology*, *33*, 09.

Zahasky, C., Kurotori, T., Pini, R., & Benson, S. M. (2019). Positron emission tomography in water resources and subsurface energy resources engineering research. *Advances in water resources*, *127*, 39–52.